Transient Diffusion and Migration to a Disk Electrode

Mark W. Verbrugge*,† and Daniel R. Baker‡

Physical Chemistry and Mathematics Departments, General Motors Research Laboratories, Warren, Michigan 48090-9055 *(Received: November 6, 1991)*

A coordinate transformation is implemented that greatly facilitates the numerical solution of the equations describing transient ionic diffusion and migration to a disk electrode. The transformed coordinates are a modified form of the classical oblate spheroidal coordinates; singularities arising at the electrode edge are removed, and the infinite model space is collapsed down to a finite rectangle. The resulting savings in storage and execution time make it feasible to do numerical calculations that were previously difficult and computationally expensive. We have applied the coordinate transformation to model transient, two-dimensional transport to a disk surface during the deposition of a metallic film. We focus our discussion on the current distribution (which determines the film thickness and uniformity of coverage), the effect of inert electrolyte, and the influence of the disk size with regard to obtaining accurate rate-constant information.

Introduction

It is now widely recognized that microelectrodes can be used to investigate charge-transfer processes at electrode–electrolyte interfaces more effectively than larger area electrodes that have been used traditionally.[1] Because it is difficult to fabricate microelectrodes to the precise dimensions required for quantitative electroanalytical work, microdisk electrodes have been the electrode geometry of choice. For construction of typical microdisk electrodes, micrometer-diameter wire of the electrode material is housed in an insulator such as borosilicate glass; the assembly is polished to form a disk electrode flush with an insulating plane. A schematic illustration of the disk system is shown in Figure 1. Experimental apparatus are available that make experimentation with such microelectrodes as routine as that for larger-area electrodes.

The chief difficulty in using microdisk electrodes for quantitative electroanalytical research is that the mathematical description of the two-dimensional transport associated with the disk system presents a substantial task, as evidenced by recent papers in this topic area. (Without attempting to be inclusive, we refer the reader to refs 2–10, and references cited therein, for recent work.) For the characterization of chemical systems with a large excess of inert electrolyte, the authors have provided a simple analytic solution[6] for the steady state if the Nernst–Planck equation[11-13] accurately describes ionic transport. If only one electrochemical reaction takes place at the electrode, the added influence of migration for reactant, product, and inert species can be treated without approximation by use of a special dependent-variable transformation, which yields a one-dimensional integral equation.[7,14] For more complex cases, however, including multiple surface and bulk reactions as well as transient mass transport, more general numerical methods such as finite differences or finite elements will most likely be the only resort.

Given the disk geometry, it is natural to do calculations in cylindrical coordinates, but achieving suitable accuracy with finite-difference or finite-element routines is difficult because of (1) the discontinuous nature of the surface boundary conditions at the electrode–insulator edge and (2) the need to address boundary conditions specified for infinite values of the radial and axial coordinates. These problems become more tractable by mapping the infinite half-plane of Figure 1 (all $r, y \geq 0$) onto a coordinate system that is more amenable to numerical solution. For the disk geometry considered here, the oblate spheroidal coordinate system[15,17] removes the edge discontinuities referred to in 1 above and was recently used by Michael et al.[4] to treat a transient diffusion equation for the disk electrode. We use a modified version of this transformation, obtained by compressing the axial coordinate so that the independent spatial variables range over finite values. As a result, the model region is transformed to a bounded rectangle with continuous boundary conditions on each edge. We will present the transport equations as they appear in this bounded domain, use them to investigate a metal-deposition reaction, and study the electrode behavior during transient diffusion and migration in tandem with interfacial electrochemical reaction. The transient problem is of interest for the study of fast electrode reactions, as will be discussed in the context of Figure 9. It is also important to understand what determines how long it takes a microelectrode to reach a steady state, a topic investigated by Zoski et al.[10] in the absence of migration. We focus our discussion on the current distribution, the effect of inert electrolyte, and the influence of the disk size with regard to obtaining accurate rate-constant information. The effect of the electrical double layer is not considered in this work; Norton et al.[16] have recently considered this matter in their treatment of a hemispherical microelectrode.

The oblate spheroidal coordinates, which form the basis of our analysis, have been applied to a variety of different problems in the past, and it is perhaps appropriate to briefly discuss some of the differences in notation and terminology which are used. The interested reader can find more details in Table 21.11 of Abramowitz and Stegun.[17] Levich[18] and Newman[19,20] refer to these

† Physical Chemistry Department.
‡ Mathematics Department.

(1) Fleischmann, M.; Pons, S.; Rolison, D.; Schmidt, P. *Ultramicroelectrodes*; Datatech Science: Morganton, NC, 1987.
(2) Bond, A. M.; Oldham, K. B.; Zoski, C. G. *J. Electroanal. Chem.* **1988**, *245*, 71.
(3) Fleischmann, M.; Daschbach, J.; Pons, S. *J. Electroanal. Chem.* **1989**, *263*, 189, 205, 225.
(4) Michael, A. C.; Wightman, R. M.; Amatore, C. A. *J. Electroanal. Chem.* **1989**, *267*, 33.
(5) Baker, D. R.; Verbrugge, M. W. *J. Electrochem. Soc.* **1990**, *137*, 1832.
(6) Baker, D. R.; Verbrugge, M. W. *J. Electrochem. Soc.* **1990**, *137*, 3836.
(7) Baker, D. R.; Verbrugge, M. W.; Newman, J. *J. Electroanal. Chem.* **1991**, *314*, 23.
(8) Cope, D. K.; Scott, C. H.; Tallman, D. E. *J. Electroanal. Chem.* **1990**, *285*, 49, 79.
(9) Taylor, G.; Girault, H. H.; McAleer, J. *J. Electroanal. Chem.* **1990**, *293*, 19.
(10) Zoski, C. G.; Bond, A. M.; Allinson, E. T.; Oldham, K. B. *Anal. Chem.* **1990**, *62*, 37.
(11) Nernst, W. *Z. Phys. Chem.* **1888**, *2*, 613. Planck, M. *Ann. Phys. Chem.* **1890**, *39*, 161.
(12) Bard, A. J.; Faulkner, L. R. *Electrochemical Methods*; Wiley: New York, 1980.
(13) Newman, J. *Electrochemical Systems*, 2nd ed.; Prentice-Hall: Englewood Cliffs, NJ, 1991.
(14) Baker, D. R. Some Nonlinear Systems of Transport Equations that can be Solved as a Single Laplace Equation; General Motors Research Publication GMR-7367; General Motors Research Laboratories: Warren, MI, 1991.
(15) Moon, P.; Spencer, D. E. *Field Theory Handbook*, 2nd ed.; Springer-Verlag: Berlin, 1971.
(16) Norton, J. D.; White, H. S.; Feldberg, S. W. *J. Phys. Chem.* **1990**, *94*, 6772.
(17) *Handbook of Mathematical Functions with Formulas, Graphs, and Mathematical Tables*; Abramowitz, M., Stegun, I. A., Eds.; NBS Applied Mathematics Series 55; National Bureau of Standards: Washington, DC, 1964; pp 751–769.

0022-3654/92/2096-4572$03.00/0

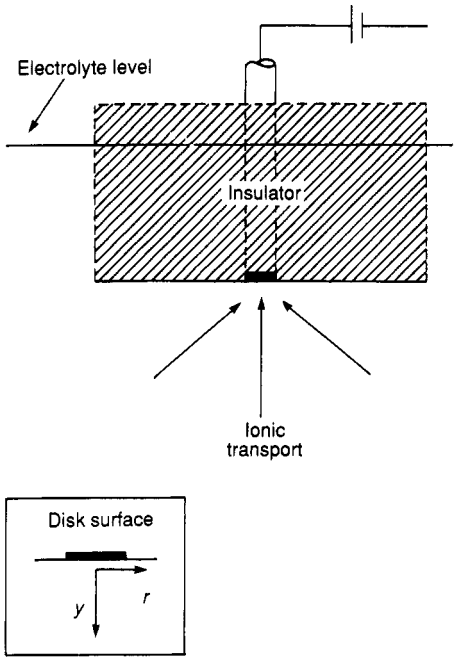

Figure 1. Schematic illustration of the disk electrode.

coordinates as (rotational) elliptic coordinates. The form they give is somewhat different from that used here (see Table 21.11 noted above for the transformation between the two), and it is not conformal. Smyrl and Newman[21] have demonstrated the utility of the rotational elliptic coordinate system for the analysis of a disk electrode using the finite-difference method. The form used in our work is conformal and is similar to that found in the book by Moon and Spencer,[15] which tabulates separable coordinate systems for different geometries. It is the same form used by Michael et al.[4] All forms share a property of particular interest to us. The transformed coordinate lines of these systems are either the lines of constant concentration or the perpendicular flux lines when transport is determined by steady-state diffusion with constant concentration along the disk. In the more general situation, when the transport equations include migration, are transient, and satisfy nonconstant boundary conditions on the electrode, concentration profiles still have roughly the same geometric form. The similarity of the coordinate system to the equiflux and equiconcentration lines in solution means that fewer nodes are necessary to discretize the problem. As already mentioned above, we have further modified these coordinates in order to map the half-infinite model space onto a finite box.

Transformed Equations

In this work, we examine metal deposition as an example application. Microelectrodes have been shown to be useful for the study of high-rate metal deposition due to the large ionic fluxes at the electrode surface.[6] The electrode reaction we model can be written as

$$O + ne^- \underset{k_a}{\overset{k_c}{\rightleftharpoons}} \text{insoluble product} \qquad (1)$$

The following subscript convention is used: 1 = reactant ion (e.g. Ag^+), 2 = unreactive ion (e.g. ClO_4^-), and 3 = unreactive ion (e.g. H^+).

The material-balance equation for each species dictates that

$$\partial c_i/\partial t = -\nabla\cdot\mathbf{N}_i \qquad (2)$$

where t denotes time and c and $\mathbf{N}$ represent species concentration and flux, respectively. Electroneutrality in solution is also assumed

$$\sum_i z_i c_i = 0 \qquad (3)$$

where z_i is the charge number of species i, and the current density $\mathbf{i}$ is given by

$$\mathbf{i} = F\sum_i z_i \mathbf{N}_i \qquad (4)$$

These three equations form the foundation of most transport models for electrochemical systems.

All that remains to complete eqs 2–4 is to give expressions for the ionic fluxes. In this work, we employ the Nernst–Planck equation:[11-13]

$$\mathbf{N}_i = \underbrace{-D_i\nabla c_i}_{\text{diffusion}} - \underbrace{z_i F u_i c_i \nabla\Phi}_{\text{migration}} \qquad (5)$$

The electric potential in solution is given by Φ. The physicochemical parameters D_i and u_i refer to the diffusion coefficient and mobility, respectively; both are taken to be constant. F represents the Faraday constant. Since convective transport is neglected in this analysis, the treatment is valid only for systems in which the disk radius is much smaller than that of the hydrodynamic boundary layer, a condition that is usually met in microelectrode investigations. Using the Nernst–Planck equation, we can rewrite the material-balance equation as

$$\partial c_i/\partial t = D_i\nabla^2 c_i + z_i F u_i \nabla\cdot(c_i\nabla\Phi), \quad i = 1, 2, 3 \qquad (6)$$

Equations 3 and 6 can be used to solve for the unknowns c_1, c_2, c_3, and Φ, once boundary conditions are specified.

At time $t = 0$ all concentrations are set to their constant bulk values

$$c_i(0,r,y) = c_i^\infty, \quad i = 1, 2, 3$$

At points far from the electrode, bulk concentrations and zero potential are specified:

$$\lim_{r+y\to\infty} c_i(t,r,y) = c_i^\infty, \quad i = 1, 2, 3$$

$$\lim_{r+y\to\infty} \Phi(t,r,y) = 0$$

On insulating surfaces, the normal fluxes are at all times zero:

$$\mathbf{N}_i\cdot\mathbf{n} = 0 \qquad i = 1, 2, 3$$

where $\mathbf{n}$ is the unit normal vector pointing into the solution. A Butler–Volmer equation is used at the electrode surface

$$\mathbf{N}_1\cdot\mathbf{n} = k_a \exp[(1-\beta)nf(E-\Phi)] - k_c c_1 \exp[-\beta nf(E-\Phi)] \quad \text{for } r \le a, \ y = 0 \qquad (7)$$

where $f = F/(RT)$ and a is the electrode radius. The electrode potential relative to a reference electrode of the same kind as that used to assess the value of Φ is given by E; β denotes a transfer coefficient; and k_a and k_c represent the anodic and cathodic rate constants, respectively. For the unreactive ions, the normal fluxes are zero on the electrode surface:

$$\mathbf{N}_i\cdot\mathbf{n} = 0 \qquad \text{for } t \ge 0, \ r \le a, \ y = 0, \ \text{and} \ i = 2, 3$$

The electroneutrality equation is also applied at the electrode surface as well as in the solution, which provides the needed fourth equation.

It will be convenient to introduce dimensionless forms of the variables and constants appearing in these equations:

$$C_i = c_i/c_1^\infty \qquad C_i^\infty = c_i^\infty/c_1^\infty$$

$$\mathcal{D}_i = D_i/D_1 \qquad \tilde{\mathbf{N}}_i = \frac{a}{D_1 c_1^\infty}\mathbf{N}_i = -[\mathcal{D}_i\tilde{\nabla}C_i + Z_i C_i\tilde{\nabla}\Psi]$$

$$V = f(E - E_e) \qquad X = r/a$$

$$Y = y/a \qquad Z_i = z_i u_i RT/D_1$$

$$\alpha = \frac{a}{D_1}k_c^{1-\beta}\left(\frac{k_a}{c_1^\infty}\right)^\beta \qquad \tau = tD_1/a^2$$

$$\Psi = f\Phi$$

(18) Levich, V. G. *Physicochemical Hydrodynamics*; Prentice-Hall: Englewood Cliffs, NJ, 1962.
(19) Newman, J. *J. Electrochem. Soc.* **1966**, *113*, 501.
(20) Newman, J. *J. Electrochem. Soc.* **1966**, *113*, 1235; **1967**, *114*, 239.
(21) Smyrl, W. H.; Newman, J. *J. Electrochem. Soc.* **1976**, *123*, 1235.

Electroneutrality eq 3 can thus be written as

$$\sum_i z_i C_i = 0$$

The equilibrium potential E_e corresponds to the electrode potential at which no current flows:

$$E_e = \frac{1}{nf} \ln\left(\frac{k_c c_1^\infty}{k_a}\right)$$

We shall scale the current densities to the steady-state diffusion limiting value

$$i_D = -\frac{4}{\pi}\frac{nFD_1 c_1^\infty}{a}$$

In addition, we use the parameter α, a measure of the mass transport to kinetic resistance:[5-7]

$$\alpha = -\frac{4}{\pi}\frac{i_{o,\infty}}{i_D}$$

where $i_{o,\infty}$ is the exchange current density based on bulk concentrations

$$i_{o,\infty} = nFk_a^\beta (k_c c_1^\infty)^{1-\beta}$$

To further elucidate the role of the dimensionless parameter α, we note that for a given chemical system, the only easily adjusted parameter in α for the experimentalist is the electrode radius a—since α is proportional to a and is the only dimensionless parameter that contains a, it is convenient to view α as a dimensionless disk radius (large disks denote large α). Thus in the plots that follow, exploring the effect of the disk radius is accomplished by varying α.

With these scalings, the dimensionless form of material-balance eq 6 and the associated boundary conditions take the form (where $\tilde{\nabla}$ means taking ∇ with respect to the scaled coordinates X and Y)

$$\partial C_i/\partial\tau = \mathcal{D}_i\tilde{\nabla}^2 C_i + Z_i\tilde{\nabla}\cdot(C_i\tilde{\nabla}\Psi), \quad \text{for } i = 1, 2, 3$$

$$C_i(0,X,Y) = \lim_{X,Y\to\infty} C_i(\tau,X,Y) = C_i^\infty, \quad \text{for } i = 1, 2, 3 \text{ and } \tau \geq 0$$

$$\lim_{X,Y\to\infty} \Psi(\tau,X,Y) = 0, \quad \text{for } \tau \geq 0$$

$$\tilde{\mathbf{N}}_i\cdot\mathbf{n} = -[\mathcal{D}_i\tilde{\nabla}C_i + Z_i C_i\tilde{\nabla}\Psi]\cdot\mathbf{n} = 0, \quad \text{for } X > 1, \ Y = 0, \text{ and all } i \text{ or } X \leq 1, \ Y = 0, \text{ and } i = 2, 3$$

$$\tilde{\mathbf{N}}_1\cdot\mathbf{n} = \alpha\{\exp[(1-\beta)n(V-\Psi)] - C_1\exp[-\beta n(V-\Psi)]\}, \quad \text{for } X \leq 1 \text{ and } Y = 0$$

As noted in the Introduction, the numerical solution of these equations is facilitated by the use of oblate spheroidal coordinates, defined by the equations

$$X = \cos(\theta)\cosh(\tilde{\Gamma}) \quad \text{and} \quad Y = \sin(\theta)\sinh(\tilde{\Gamma}) \qquad (8)$$

This coordinate transformation maps the half-space of points with $y \geq 0$ to the half-infinite strip with $0 \leq \theta \leq \pi/2$ and $0 \leq \tilde{\Gamma} < \infty$. (The coordinate $\tilde{\Gamma}$ corresponds to Γ used by Michael et al.[4] to model transient diffusion to a disk electrode with the oblate spheroidal coordinates, and the θ coordinate of this work is identical to that used by Michael et al.[4]) To compress this half-infinite strip onto a finite box, we introduce the coordinate Γ:

$$\Gamma = \frac{\tilde{\Gamma}}{1+\tilde{\Gamma}}$$

The transformation in terms of θ and Γ is now given by

$$X = \cos(\theta)\cosh\left(\frac{\Gamma}{1-\Gamma}\right) \quad \text{and} \quad Y = \sin(\theta)\sinh\left(\frac{\Gamma}{1-\Gamma}\right) \qquad (9)$$

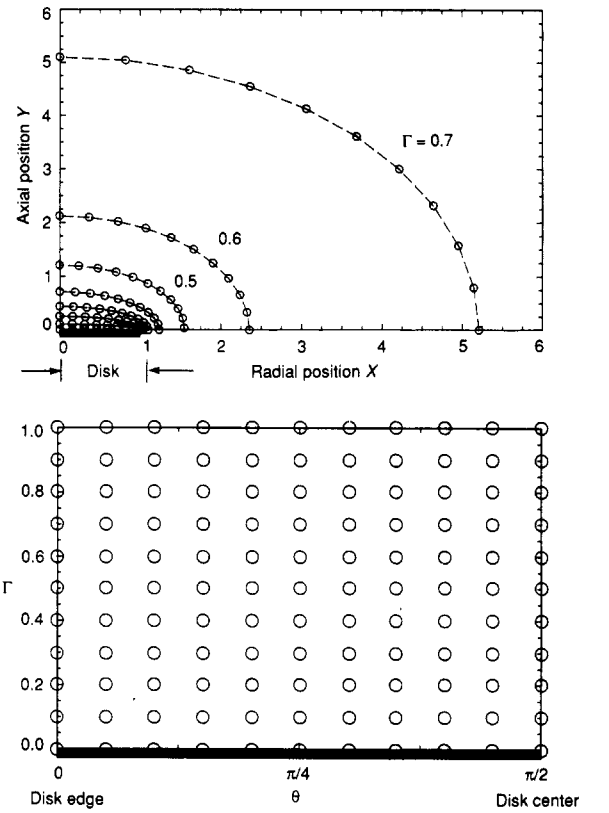

Figure 2. Botton panel: New coordinate system with an 11 × 11 equally spaced mesh. The coordinate system may be viewed as a compressed form of the oblate spheroidal system.[15,17] Top panel: Disk electrode and associated cylindrical coordinates X and Y. (The problem is rotationally symmetric.) Shown on the top panel are the node placements corresponding to the mesh depicted in the lower panel.

Using this transformation, one can map the half-space of points with $Y \geq 0$ onto the rectangle with $0 \leq \theta \leq \pi/2$ and $0 \leq \Gamma \leq 1$ (as indicated in the plots of Figure 2, which shall be discussed in the next section).

With these definitions, the following transformed version of the material-balance equation is derived in the Appendix:

$$\left[\sin^2(\theta) + \sinh^2\left(\frac{\Gamma}{1-\Gamma}\right)\right]\frac{\partial C_i}{\partial\tau} = \mathcal{D}_i\left\{\frac{\partial^2 C_i}{\partial\theta^2} - \tan(\theta)\frac{\partial C_i}{\partial\theta} + (1-\Gamma)^4\frac{\partial^2 C_i}{\partial\Gamma^2} + \left[(1-\Gamma)^2\tanh\left(\frac{\Gamma}{1-\Gamma}\right) - 2(1-\Gamma)^3\right]\frac{\partial C_i}{\partial\Gamma}\right\} + Z_i\left(C_i\left\{\frac{\partial^2\Psi}{\partial\theta^2} - \tan(\theta)\frac{\partial\Psi}{\partial\theta} + (1-\Gamma)^4\frac{\partial^2\Psi}{\partial\Gamma^2} + \left[(1-\Gamma)^2\tanh\left(\frac{\Gamma}{1-\Gamma}\right) - 2(1-\Gamma)^3\right]\frac{\partial\Psi}{\partial\Gamma}\right\} + \frac{\partial C_i}{\partial\theta}\frac{\partial\Psi}{\partial\theta} + (1-\Gamma)^4\frac{\partial C_i}{\partial\Gamma}\frac{\partial\Psi}{\partial\Gamma}\right) \quad \text{for } i = 1, 2, 3 \qquad (10)$$

The region for which these equations will be solved corresponds to the space X, $Y \geq 0$, or $0 \leq \theta \leq \pi/2$ and $0 \leq \Gamma \leq 1$. There are thus four boundary components which must be considered: the electrode surface, $Y = 0$ and $0 \leq X \leq 1$ ($\Gamma = 0$ and $0 \leq \theta \leq \pi/2$); the insulating container wall, $Y = 0$ and $X > 1$ ($\theta = 0$ and $0 < \Gamma \leq 1$); the line of symmetry through the center of the disk, $X = 0$ ($\theta = \pi/2$ and $0 < \Gamma \leq 1$); and the region where X and Y tend to ∞ ($\Gamma \to 1$ and $0 \leq \theta \leq \pi/2$). Boundary conditions in cylindrical coordinates have been given for all components except the line $X = 0$ through the center of the electrode disk, where by rotational symmetry the radial component of the fluxes must vanish. Expressions for the normal components of the fluxes on the boundary components are given in the Appendix, and they yield the following initial and boundary conditions:

$$C_i(0,\theta,\Gamma) = \lim_{\Gamma\to 1} C_i(\tau,\theta,\Gamma) = C_i^\infty$$

for $i = 1, 2, 3$ and $\tau \geq 0$

$$\lim_{\Gamma\to 1} \Psi(\tau,\theta,\Gamma) = 0 \qquad \text{for } \tau \geq 0$$

$$\mathcal{D}_i \frac{\partial C_i}{\partial \theta} + Z_i C_i \frac{\partial \Psi}{\partial \theta} = 0 \qquad \text{for } \theta = 0, \pi/2 \text{ and all } i$$

$$\mathcal{D}_i \frac{\partial C_i}{\partial \Gamma} + Z_i C_i \frac{\partial \Psi}{\partial \Gamma} = 0 \qquad \text{for } \Gamma = 0 \text{ and } i = 2, 3$$

$$-\frac{1}{\sin(\theta)}\left(\frac{\partial C_1}{\partial \Gamma} + Z_1 C_1 \frac{\partial \Psi}{\partial \Gamma}\right) = \alpha\{\exp[(1-\beta)n(V-\Psi)] - C_1 \exp[-\beta n(V-\Psi)]\} \qquad \text{for } \Gamma = 0 \quad (11)$$

We now address the calculation of the average current density. Using expression A8 given in the Appendix for the normal flux on the electrode and the fact that

$$\mathbf{N}_1 \cdot \mathbf{n} = i/nF$$

we can write

$$\frac{i}{i_D} = \frac{\pi}{4\sin(\theta)}\left(\frac{\partial C_1}{\partial \Gamma} + Z_1 C_1 \frac{\partial \Psi}{\partial \Gamma}\right) \qquad (12)$$

which is embodied in the boundary condition of eq 11. The average scaled current density is obtained by surface integration of eq 12:

$$\frac{i_{av}}{i_D} = 2\int_0^1 \frac{i}{i_D} X\, dX = \frac{\pi}{2}\int_0^{\pi/2}\left(\frac{\partial C_1}{\partial \Gamma} + Z_1 C_1 \frac{\partial \Psi}{\partial \Gamma}\right)\cos(\theta)\, d\theta$$

For numerical calculations, the material-balance equation for species 3 was combined with the electroneutrality equation, resulting in three equations for the three unknowns C_1, C_2, and Ψ. These equations were solved by the finite-difference method. By comparing our steady-state calculations with the integral-transform solution to the steady-state version of this problem,[7] we found that a grid consisting of 31 equally spaced mesh points in the θ coordinate and 21 equally spaced mesh points in the Γ coordinate yielded sufficient accuracy for steady-state analyses (usually less than a 1% difference between the two methods was observed). The accuracy of the transient behavior of the solutions depends on the grid spacing of both the space and time dimensions, and Figure 3 gives an indication of what accuracy can be expected for problems of this type. Using different grid spacings, average currents as a function of dimensionless time were calculated for a well-supported system ($C_1 \ll C_2$) and a potential step to $V = -6$. Under these conditions, the potential Ψ in Butler–Volmer eq 11 goes to zero, the migration terms in the flux go to zero as well, and the current can be calculated from a single transient diffusion equation in C_1. The resulting single equation reduces the amount of time and memory required for finer grid calculations, allowing one to see how the calculations converge as grid size decreases. Shown in the top panel of Figure 3 are results for short times, and the bottom panel displays results for longer times. The accuracy of the 21 × 21 grid results of Figure 3 are indicative of the accuracy of the analyses in the Results section. For the full coupled, nonlinear problem, we found that coarse grids (e.g., 11 × 11 grids) often gave trouble with regard to convergence of the Newton–Raphson iteration. Convergence was easier to obtain with a larger number of mesh points along the disk surface, which is why 31 mesh points were used in the θ direction and 21 in the Γ direction for our analyses.

The plots of Figure 2 give an indication of why the compressed, oblate spheroidal coordinate system admits accurate numerical analysis for the disk system. A slightly different form of these

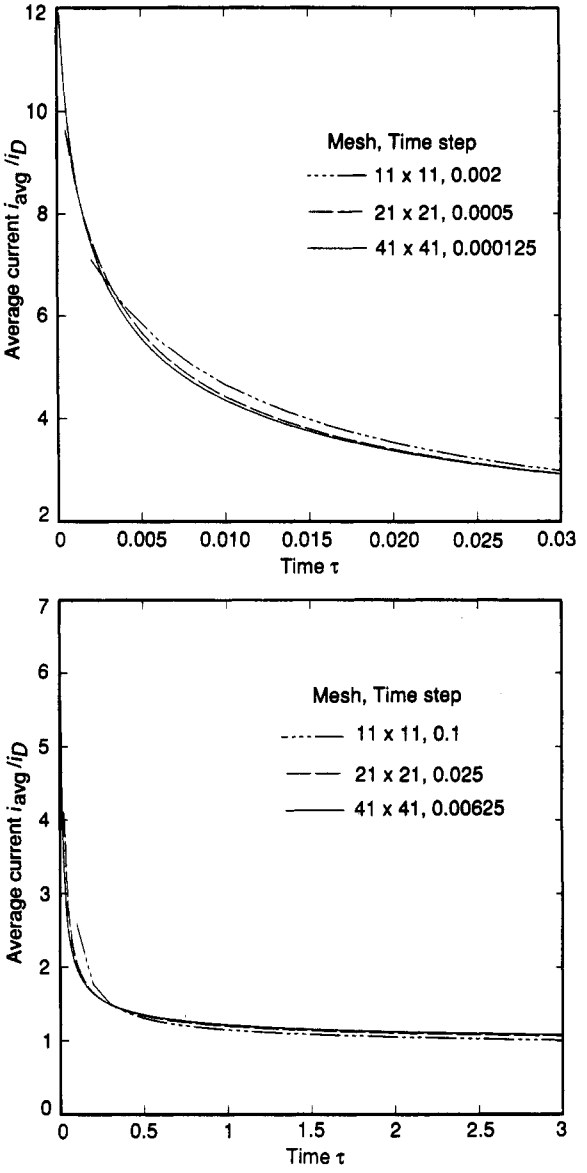

Figure 3. Grid and time-step analysis. The dimensionless average current (i_{av}/i_D) is plotted as a function of the dimensionless time (τ). Top panel: Short-time results. Bottom panel: Long-time results. The mesh points in the Γ and θ direction and the time-step size ($\Delta\tau$) are indicated. For this plot, $C_2^\infty \gg 1$ and $V = -6$. All other conditions are given in Table I.

TABLE I: Base-Case Parameter Values

C_2^∞	1.0[a]	z_1 and Z_1	1.0[b]	α	1.0
$\mathcal{D}_2$, $\mathcal{D}_3$	1.0	z_2 and Z_2	1.0[b]	β	0.5
n	1.0	z_3 and Z_3	−1.0[b]		

[a] By electroneutrality, $C_3^\infty = 2$. [b] $Z_i = z_i$ assumes the Nernst–Einstein relation, $D_i = u_i RT$.

plots can be found in the work of Michael et al.[4] Shown in the lower panel is an example of a finite-difference mesh using 11 nodes in each direction. The upper panel maps these mesh points back onto the cylindrical coordinate system; curves of constant Γ are depicted. The mesh-point density is highest near the electrode–insulator boundary; farther from the disk, the nodal density is decreased and curves of constant Γ begin to take on a circular-arc appearance. We are not able to show curves in the top panel for $\Gamma > 0.7$ without going to larger values of X and Y, which would obscure the important features near the electrode surface. Although this variable density of mesh points gives some idea of why calculations in the transformed coordinates are more efficient, it is also worth noting that doing numerical calculations in the transformed coordinates is not equivalent to doing calculations in cylindrical coordinates with the corresponding variable

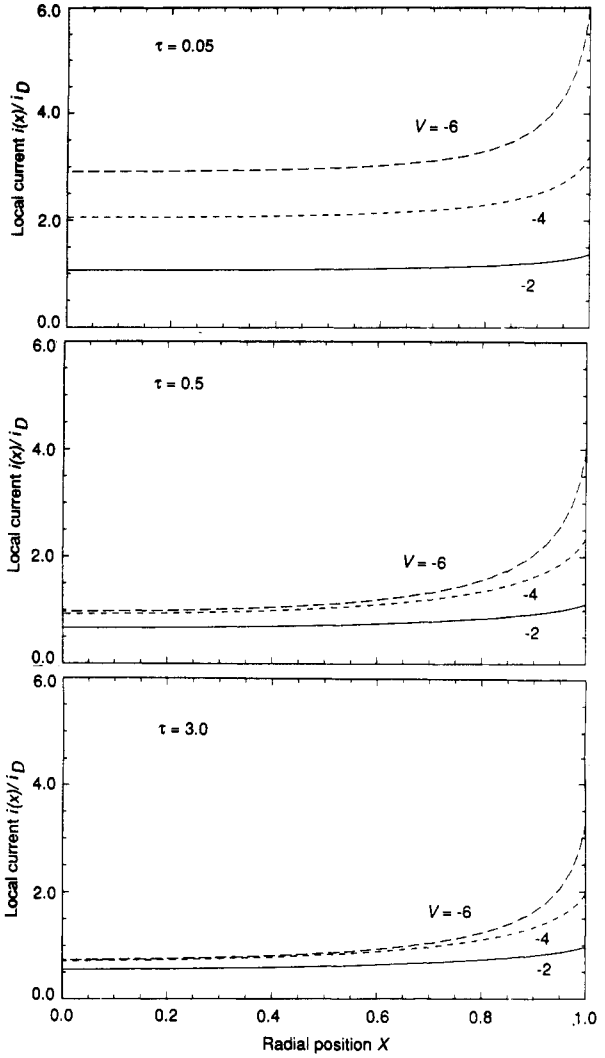

Figure 4. Current distributions $i(X)/i_D$ for various times τ and electrode potentials V. The potential was stepped from its open-circuit value to V at time zero.

grid spacing. For example, it is known (see the discussion at the end of the next section) that at steady-state limiting current conditions the current distribution in cylindrical coordinates has a square root singularity at the disk edge, and a finite number of mesh points cannot capture this behavior. In the transformed coordinates, this same current distribution becomes constant and can thus be exactly represented with few mesh points.

Results

In order to understand the nature of transient migration and diffusion to a disk electrode, we investigate the metal-deposition reaction of eq 1. The values of Table I are used to form our base case. Reasonable parameter values of many real chemical systems yield dimensionless-group values similar to those of Table I; the values of Table I were also chosen for a base case because they correspond to a situation wherein both migration and diffusion contribute significantly to transport, and resistance due to mass-transport, ohmic, and interfacial-kinetic phenomena are important.

Potential Step. Perhaps the easiest experiment to analyze is a potential step from an initial condition corresponding to an open circuit. The results of Figures 4–7 represent such an experiment. The current-distribution results are shown in Figure 4 for dimensionless potential values V of −2, −4, and −6 and dimensionless times τ of 0.05, 0.5, and 3.0. Initially, the current distribution is identical to that of the secondary current distribution.[13,20] That is, before the concentrations are altered from their bulk values, the Laplace equation applies for the electric potential and the Butler–Volmer equation can be used with constant concentrations.

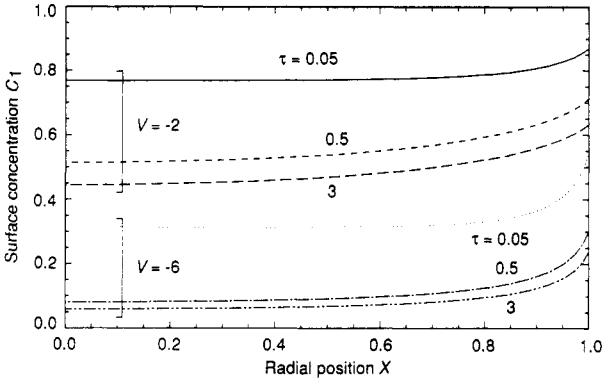

Figure 5. Surface concentration distributions $C_1(\tau,X,0)$ corresponding to the plots of Figure 4.

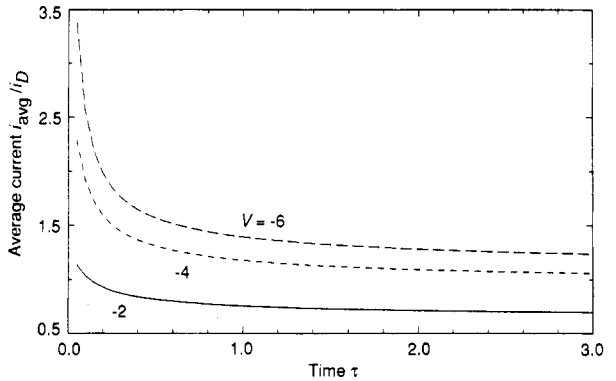

Figure 6. Average current i_{av}/i_D corresponding to the plots of Figures 4 and 5.

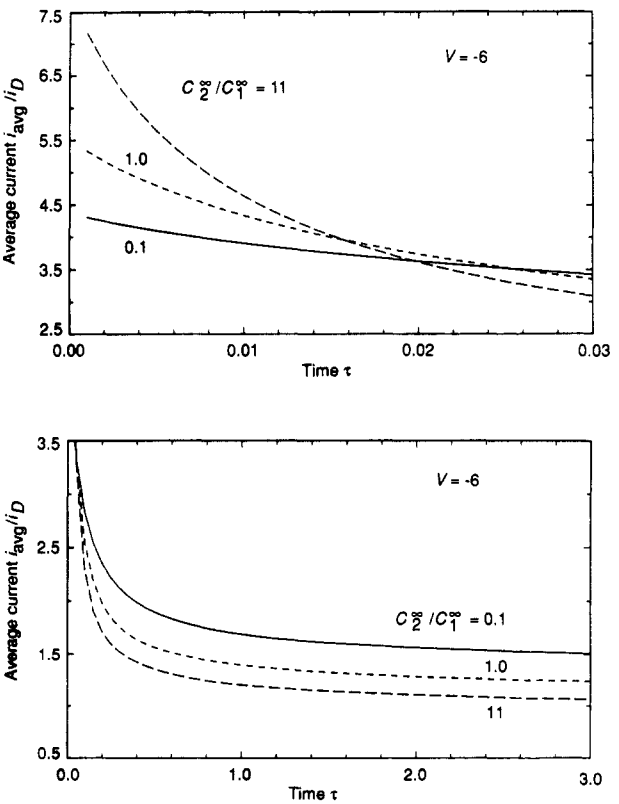

Figure 7. Effect of supporting electrolyte (represented by the parameter c_2^∞/c_1^∞) on the average current (i_{av}/i_D) response.

This can be seen by considering the equation for conservation of the total charge, which, by electroneutrality, takes the form

$$\nabla\cdot[\sum_i z_i D_i \nabla c_i + (\sum_i z_i^2 F u_i c_i)\nabla\Phi] = 0$$

For small τ, the gradients of the concentrations will be negligible

outside of a thin boundary layer around the electrode, so that the above equation reduces to a simple Laplace equation in the potential Φ, or its scaled form Ψ. Note that the potential gradients create fluxes in all three species, even though the boundary conditions stipulate that the normal fluxes for the supporting electrolyte must vanish along the electrode. It follows that the concentrations of species 2 and 3 must change in the boundary layer at the electrode surface, and, by electroneutrality, this causes a change in the concentration c_1 of the reacting species as well. As τ increases, so does the magnitude of the concentration changes at the electrode surface, as well as the thickness of the region of nonconstant concentrations near the electrode. Once these concentration changes become significant, the secondary current distribution no longer prevails; until that time, the system behavior is dictated by an ohmic drop throughout the electrolyte solution and by charge-transfer processes at the electrode–electrolyte interface. When the secondary current distribution prevails, the uniform current distribution is obtained as the solution becomes well supported ($c_1^\infty/c_2^\infty \rightarrow 0$). This is because the potential in solution Ψ tends to zero, and the average current density is given by

$$\lim_{\tau\rightarrow 0}\left(\frac{i_{av}}{i_D}\right) = -\alpha\frac{\pi}{4}\{\exp[(1-\beta)nV] - \exp[-\beta nV]\} \qquad c_1^\infty/c_2^\infty \rightarrow 0 \quad (13)$$

More generally, the right-hand side of eq 13 provides a bound on the current density at all times for the conditions in this work. At the other extreme, as $\tau \rightarrow \infty$ and $V \rightarrow -\infty$, the primary current distribution is obtained, which corresponds to maximum nonuniformity.[13,19]

A discussion of the factors influencing the steady-state current distribution associated with the reaction of eq 1 was given in previous work,[7] and some of the same observations carry over to the transient analysis. In particular, for small values of α the current distribution tends to become uniform at all times τ. The primary current distribution observed for large negative voltages near steady-state conditions also arises for large values of α and small voltages; as the voltage becomes more negative, the nonuniformity of the current distribution increases. Thus the plots of Figure 4 show nearly uniform current distributions for small electrode potential values and increasing nonuniformity for larger negative values of V. The surface concentration profiles corresponding to the current-distribution results of Figure 4 are given in Figure 5; shown are plots for the smallest and largest magnitudes of the electrode potential, $V = -2$ and -6, respectively. The general form of the surface-concentration profiles is similar to that of the current distribution. The more accessible edge region of the disk obtains larger current densities and reactant concentrations. Contrary to the current distribution, however, the surface concentration of the lone reactant will be uniformly zero under steady-state limiting current conditions ($\tau \rightarrow \infty$ and $V \rightarrow -\infty$). As shown in Figure 6, the average current density undergoes a large change for dimensionless times less than unity and asymptotes to its steady-state value for longer times; the steady-state results correspond to the integral-transform results generated in ref 7 for this system.

The effect of migration is demonstrated in Figure 7 for an electrode bias of $V = -6$. The lower panel shows results corresponding to longer times; these results are similar to the steady-state analysis for this system—as the supporting electrolyte concentration is decreased, corresponding to smaller values of c_2^∞/c_1^∞, larger currents result due to the increased effect of ionic migration. The results of Figure 7 indicate that, for the case of excess inert electrolyte ($c_2^\infty/c_1^\infty = 11$) and long times, the average current nears the limiting current for a well-supported solution, i.e., $i_{av}/i_D \rightarrow 1$. As was mentioned in the discussion of Figure 4, for very short times the species concentrations are nearly constant along the electrode surface and the secondary current distribution prevails. Under these conditions, the influence of supporting electrolyte is to increase the average current i_{av}/i_D by decreasing the electrolyte ohmic resistance (Ψ tends to zero as the supporting electrolyte is increased).[13,20] The upper panel of Figure 7 contains calculations in this shorter time regime and shows that the curves cross at a dimensionless time near 0.02. The case corresponding to the largest amount of inert electrolyte ($c_2^\infty/c_1^\infty = 11$) yields the highest initial average current density. To underscore the results of Figure 7, we note that the addition of supporting electrolyte introduces two different effects. It increases the electrolyte conductivity but also decreases the electric fields which drive migrational transport of the reactant. At short times, the first effect dominates, causing an increase in the average current, whereas at long times, the second effect dominates and causes a decrease in the average current.

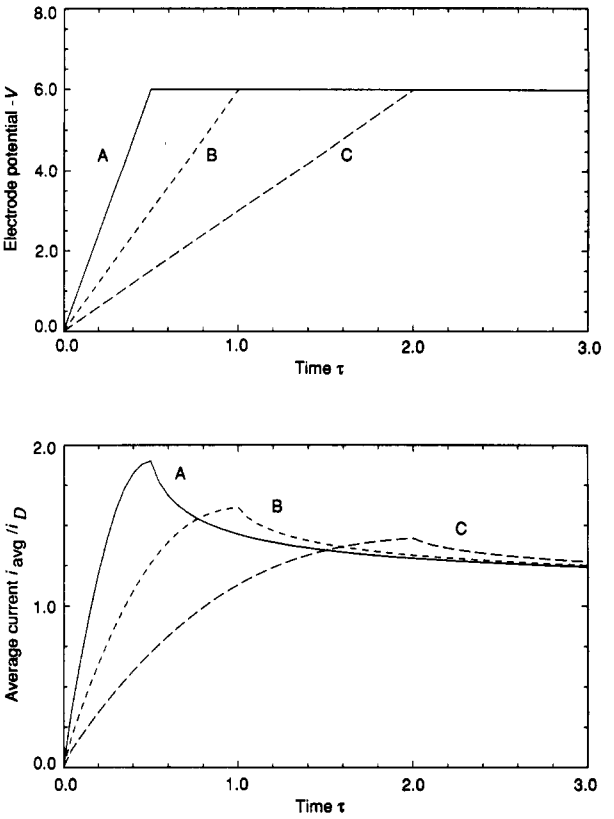

Figure 8. Potential ramp experiment. Top panel: Electrode potential source (V) versus time. Bottom panel: Average-current (i_{av}/i_D) response for different potential sources.

Potential Ramp. A second commonly employed chronopotentiometry technique involves the use of a ramped potential source, such as that shown in the top panel of Figure 8. This technique is particularly useful for the study of fast electrode reactions. Shown in the bottom panel of Figure 8 are current responses to the three potential regimes of the top panel. The ramp durations are all of the order of the characteristic time for mass transport, a^2/D_1. For shorter ramp times, the resistance to mass transport is reduced over the ramp time relative to the interfacial charge-transfer resistance, which allows for more accurate kinetic studies. The peak average current is highest for case A and lowest for case C, reflecting that faster potential ramps yield higher peak currents. For very slow potential ramps, the average-current response would be identical in form to the potential response; i_{av} would vary linearly with time during the potential ramp and maintain a constant value after the ramp duration.

The utility of the ramped potential source for the investigation of fast electrode reactions is evident in Figure 9. In the steady-state analysis of this system,[7] it was shown that, for values of α greater than 2, accurate kinetic measurements cannot be obtained. In contrast, the transient analysis depicted in Figure 9 shows that, for a potential-ramp time corresponding to the characteristic time for transport, resulting in a dimensionless ramp time of unity, the average-current response is strongly dependent on the value of α for $\alpha \leq 10$. For shorter ramp times, a greater sensitivity to the value of α is obtained, and more accurate kinetic

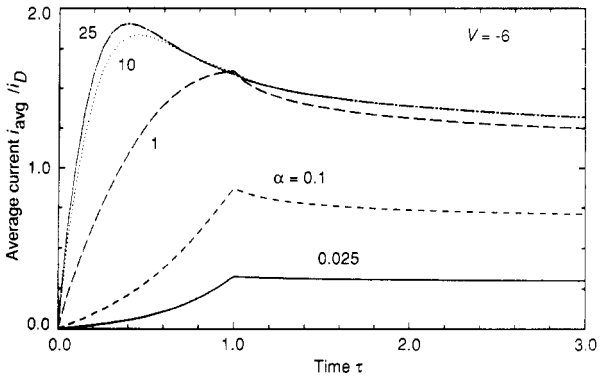

Figure 9. Influence of mass-transport resistance to kinetic resistance on the average-current (i_{av}/i_D) response. Note that $\alpha = -4i_{o,\infty}/(\pi i_D)$, where $i_{o,\infty}$ is the exchange current density based on bulk concentrations and i_D is the diffusion-limiting current density.

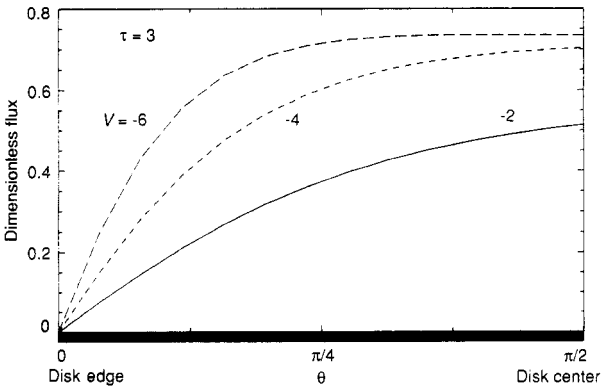

Figure 10. Dimensionless flux $[\partial C_1/\partial\Gamma + Z_1C_1(\partial\Psi/\partial\Gamma)]$ versus position for various electrode potentials V and $\tau = 3$ (near steady-state conditions). These curves correspond to the potential-step current distributions shown in the lowest panel of Figure 4.

measurements can be made. For very short ramp times, double-layer charging can influence significantly the current–potential relationship, although such capacitive effects become noticeable only if unusually short potential-ramp times are employed,[22,23] since microelectrodes in general reduce the influence of double-layer charging. (These capacitive effects are not included in the calculations.) For very small microelectrodes, sometimes referred to as nanodes,[24] the thickness of the electric double may be similar to that of the characteristic electrode length, and the potential drop across the double-layer region must be included in analyzing the microelectrode system.[16] The dimensionless peak average current is a function of the parameter α; larger values of α, corresponding to faster reactions or smaller diffusion-limiting current densities, yield larger peak values of i_{av}/i_D. In addition, larger values of α shift the maximum in the dimensionless-current-versus-time curve to shorter times. These observations can be understood by recognizing that fast reaction rates will yield larger currents prior to the onset of mass-transport limitations. Since the secondary current distribution prevails before concentration variations exist, larger values of α yield larger initial values of i_{av}/i_D; consequently, the effects of mass-transport limitations are observed sooner in the $i_{av}/i_D - \tau$ response, as the electrolyte layer near the electrode surface is depleted sooner of the reactant which is required to produce the current.

Attributes of the Coordinate Transformation. The coordinate transformation we have employed can be used to simulate a variety of electrochemical experiments with microdisk electrodes. The most obvious advantage of the transformed system relative to the cylindrical coordinate system is that we are able to replace a boundary value problem on an infinite half-plane, with discontinuous boundary conditions at the disk edge, with a new problem on a rectangular domain that contains none of the original discontinuities on the boundaries. Using Figures 10–13, we are able to note other aspects of the transformed problem that help to explain the success obtained with the transformed coordinate system.

It is known that the limiting current distribution for the steady-state problem is given by

$$i(r)/i_{av} = 0.5/[1 - (r^2/a^2)]^{1/2}$$

even if migrational effects are present;[7] the infinite currents that occur at the disk edge create difficulties if one tries to solve the model equations in cylindrical coordinates. From eq 12, however,

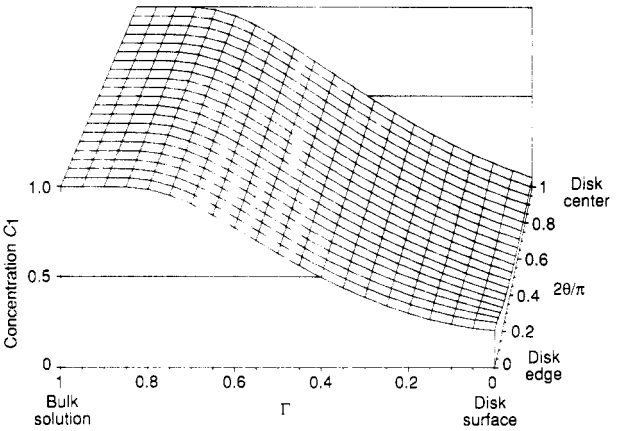

Figure 11. Concentration $C_1(\infty,\theta,\Gamma)$ in the compressed, oblate spheroidal coordinate system. (Note that both axes are plotted so as to range between 0 and 1.)

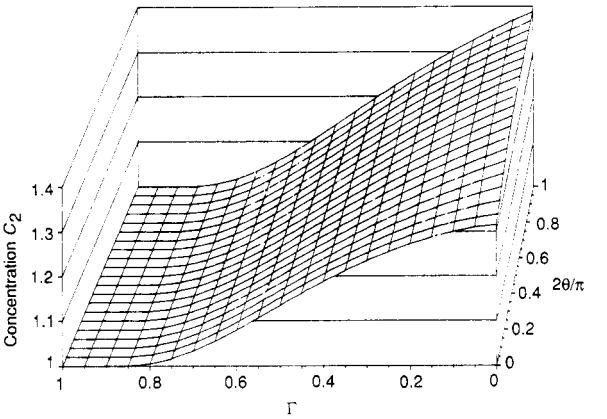

Figure 12. Concentration $C_2(\infty,\theta,\Gamma)$ in the compressed, oblate spheroidal coordinate system.

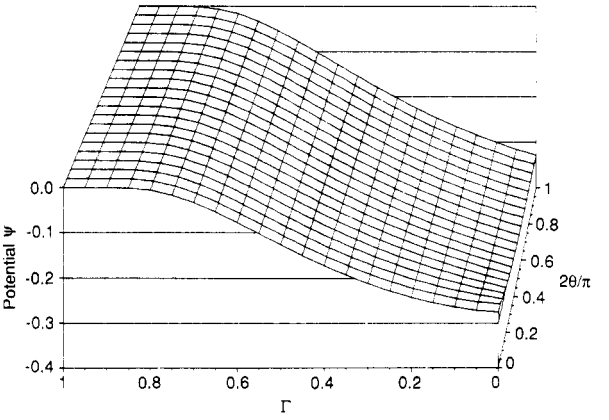

Figure 13. Potential $\Psi(\infty,\theta,\Gamma)$ in the compressed, oblate spheroidal coordinate system corresponding to the steady-state results of Figures 11 and 12.

(22) Andrieux, C. P.; Garreau, D.; Hapiot, P.; Savéant, J. M. *J. Electroanal. Chem.* **1988**, *248*, 4473.
(23) Wipf, D. O.; Michael, A. C.; Wightman, R. M. *J. Electroanal. Chem.* **1989**, *269*, 15.
(24) Penner, R. M.; Heben, M. J.; Longin, T. L.; Lewis, N. S. *Science* **1990**, *250*, 1118.

$$\frac{\partial C_1}{\partial \Gamma} + Z_1 C_1 \frac{\partial \Psi}{\partial \Gamma} = \frac{4 \sin(\theta)}{\pi} \frac{i}{i_D} \quad (14)$$

and one can show that under steady-state limiting-current conditions the left side of the above equation becomes constant. Thus near the limiting current, the nearly constant derivatives in the oblate spheroidal coordinates can be captured numerically using fewer nodes than would be necessary in cylindrical coordinates.

The phenomenon of large currents at the disk edge is observable both for large disks and large negative voltages, as shown in the current distributions of Figure 4. Figure 10 shows the same distributions shown in the bottom panel of Figure 4, but now the flux expression appearing on the left-hand side of eq 14 is plotted instead. Because of the factor sin (θ) in eq 14, this flux expression goes to zero at the disk edge, where $\theta = 0$. Furthermore, as evidenced by the comparison of the lowest panel of Figure 4 with Figure 10, the curvature in the dimensionless flux versus position is more pronounced in the cylindrical coordinate system, which can also lead to greater numerical difficulties.

Three-dimensional surface plots for the dependent variables C_1, C_2, and Ψ are shown in Figures 11–13 respectively. These plots are for the steady-state condition with $V = -6$. The annotations of Figure 11 identify the disk center and edge and the boundary at infinity. It is quite apparent that the surface contours are all rather smooth, indicating that numerical methods can be used to approximate accurately the solutions to these variables. As was noted at the end of the previous section, if one were to use simply the coordinate locations shown in the top panel of Figure 2 with a variable mesh point scheme and solve the problem in the X–Y system (assuming that large values of X and Y are employed to mimic the infinity conditions), accuracy equal to that for the transformed coordinate system should not be expected. This is because the second-order approximations employed in the calculation of finite-difference derivatives will in general lead to greater errors in the X–Y coordinate system relative to the θ–Γ system.

Conclusions

Using a coordinate transformation, we have modeled the disk electrode subject to nonlinear, transient mass transport and accompanying electrochemical reaction. The coordinate transformation amounts to mapping the electrode, the coplanar insulator, and the adjacent infinite reservoir of electrolyte onto a rectangular region, which removes singularities arising at the electrode edge and collapses the infinite model space down to a finite rectangle. The resulting savings in storage and execution time make it feasible to do numerical simulations with more general numerical methods, such as finite differences or finite elements, that would otherwise be prohibitively expensive.

We have applied the coordinate transformation to model transient mass transport to a disk surface during the deposition of a metallic film. Our simulation results indicate that many of the conclusions reached for the steady-state analysis of this problem[7] apply to the transient analysis. Specifically, the parameter α,

$$\alpha = -\frac{4 i_{0,\infty}}{\pi i_D}$$

which is a measure of the mass-transport resistance (reflected by the inverse of the diffusion-limiting current density i_D) to that of kinetics (as embodied in the inverse of the exchange current density $i_{0,\infty}$), plays a major role in determining the average current and the current distribution. For a given chemical system, with specified electrode materials and bulk solution concentrations, only the electrode potential (or average current) and the disk radius may be altered by the researcher; in the dimensionless form of the steady-state and transient equations, only the dimensionless parameter α is affected by the disk radius (through the value of i_D). In agreement with the steady-state analysis, smaller values of α yield (1) a more uniform current distribution and (2) a higher sensitivity to charge-transfer rate constants. The primary advantage to using transient techniques is that α need not be as small in order to make accurate kinetic measurements, as evidenced by the potential scan results of Figure 9.

A distinguishing difference between the steady-state and transient analyses is the effect of inert (or supporting) electrolyte. The steady-state analysis shows that inert electrolyte serves to diminish migrational transport by reducing the electric field strength, which leads to reduced current densities. The same trend is observed in the present work for longer times. The transient analysis shows that for times significantly shorter than the characteristic time constant for mass transport, however, the primary effect of inert electrolyte is to increase the solution conductivity, which leads to increased current densities. Thus if nonlinear migration is neglected in metal-deposition studies (cf. eq 1), then the calculated average current will exceed the actual current for short times and underestimate the average current for long times.

List of Symbols

a	disk-electrode radius, cm
c	concentration, mol/cm^3
C_i	dimensionless concentration c_i/c_1^∞
D	diffusion coefficient, cm^2/s
$\mathcal{D}_i$	dimensionless diffusion coefficient D_i/D_1
E	electrode potential, V
f	F/RT, V^{-1}
F	Faraday's constant, 96 487 C/equiv
i	normal current density at the disk surface, A/cm^2
$\mathbf{i}$	current density, A/cm^2
i_D	diffusion limited current density, $-4nFD_1c_1^\infty/(\pi a)$
$i_{0,\infty}$	exchange current density based on bulk concentrations, A/cm^2
k_a	anodic rate constant, mol/(cm^2·s)
k_c	cathodic rate constant, cm/s
n	number of electrons in reaction, equiv/mol
$\mathbf{n}$	unit normal vector pointing into solution
r	radial position, cm
R	gas constant, 8.314 J/(mol·K)
t	time, s
T	temperature, K
u	ionic mobility, (mol·cm^2)/(J·s)
V	dimensionless electrode potential $f(E - E_e)$
X	dimensionless radial coordinate, r/a
Y	dimensionless axial coordinate, y/a
y	axial coordinate, cm
z	charge number, equiv/mol
Z_i	$z_i u_i RT/D_1$
Greek Letters	
α	$-4i_{0,\infty}/(\pi i_D)$
β	transfer coefficient of reaction
Γ	normal coordinate in transformed space
θ	tangential coordinate in transformed space
τ	dimensionless time, tD_1/a^2
Φ	electrical potential in solution, V
Ψ	dimensionless electrical potential in solution $f\Phi$
Subscripts	
e	equilibrium
i	species i
∞	evaluated far from the electrode surface

Appendix: The Coordinate Transformation

In this appendix we will give the details of the transformed material balance equation (6) when the potential and all concentrations depend on the radial and axial cylindrical coordinates r and y only; i.e., they have no dependence on the angular coordinate. In terms of the scaled variables (see the List of Symbols for definitions), this equation takes the form

$$\frac{\partial C_i}{\partial \tau} = \frac{1}{X}\frac{\partial}{\partial X}\left[X\left(\mathcal{D}_i \frac{\partial C_i}{\partial X} + Z_i C_i \frac{\partial \Psi}{\partial Y}\right)\right] + \frac{\partial}{\partial Z}\left[\mathcal{D}_i \frac{\partial C_i}{\partial Y} + Z_i C_i \frac{\partial \Psi}{\partial Y}\right] \quad (A1)$$

We compute the transformed version of this equation in two steps:

first by expressing it in terms of the oblate spheroidal coordinates θ and $\tilde{\Gamma}$ (given by eq 8) and then transforming the result into the coordinates θ and Γ given by eq 9.

For step 1, the chain rule can be used to write

$$\begin{pmatrix} \partial/\partial\theta \\ \partial/\partial\tilde{\Gamma} \end{pmatrix} = \begin{bmatrix} \partial X/\partial\theta & \partial Y/\partial\theta \\ \partial X/\partial\tilde{\Gamma} & \partial Y/\partial\tilde{\Gamma} \end{bmatrix} \begin{pmatrix} \partial/\partial X \\ \partial/\partial Y \end{pmatrix}$$

and by inverting this matrix equation, one obtains

$$\frac{\partial}{\partial X} = a_{11}\frac{\partial}{\partial\theta} + a_{12}\frac{\partial}{\partial\tilde{\Gamma}}$$

$$\frac{\partial}{\partial Y} = a_{21}\frac{\partial}{\partial\theta} + a_{22}\frac{\partial}{\partial\tilde{\Gamma}} \tag{A2}$$

where

$$\begin{bmatrix} a_{11} & a_{12} \\ a_{21} & a_{22} \end{bmatrix} = \frac{1}{\det}\begin{bmatrix} -\cosh(\tilde{\Gamma})\sin(\theta) & \sinh(\tilde{\Gamma})\cos(\theta) \\ \sinh(\tilde{\Gamma})\cos(\theta) & \cosh(\tilde{\Gamma})\sin(\theta) \end{bmatrix}$$

and

$$\det = \cosh^2(\tilde{\Gamma})\sin^2(\theta) + \sinh^2(\tilde{\Gamma})\cos^2(\theta)$$

$$= \sinh^2(\tilde{\Gamma}) + \sin^2(\theta)$$

Second derivatives in X and Y can be calculated as derivatives in θ and $\tilde{\Gamma}$ by applying the expressions in eq A2 to themselves; the matrix elements a_{ij} must also be differentiated when this is done. The transformed version of eq A1 is, however, easier to obtain by noting that eq A1 can be written as

$$\partial C_i/\partial\tau = \mathcal{D}_i\nabla^2 C_i + Z_i C_i \nabla^2\Psi + Z_i \nabla C_i \cdot \nabla\Psi \tag{A3}$$

where

$$\nabla^2 C_i = \frac{1}{X}\frac{\partial}{\partial X}\left(X\frac{\partial C_i}{\partial X}\right) + \frac{\partial^2 C_i}{\partial Y^2}$$

$$= \frac{1}{\det}\left[\frac{\partial^2 C_i}{\partial\theta^2} + \frac{\partial^2 C_i}{\partial\tilde{\Gamma}^2} + \tanh(\tilde{\Gamma})\frac{\partial C_i}{\partial\tilde{\Gamma}} - \tan(\theta)\frac{\partial C_i}{\partial\theta}\right] \tag{A4}$$

Using eq A2, one also finds that

$$\nabla C_i \cdot \nabla\Psi = \frac{\partial C_i}{\partial X}\frac{\partial\Psi}{\partial X} + \frac{\partial C_i}{\partial Y}\frac{\partial\Psi}{\partial Y}$$

$$= \frac{1}{\det}\left[\frac{\partial C_i}{\partial\theta}\frac{\partial\Psi}{\partial\theta} + \frac{\partial C_i}{\partial\tilde{\Gamma}}\frac{\partial\Psi}{\partial\tilde{\Gamma}}\right] \tag{A5}$$

To complete the calculation, all that remains is step 2, i.e., to transform the $\tilde{\Gamma}$ coordinate to the Γ coordinate, where

$$\Gamma = \frac{\tilde{\Gamma}}{1+\tilde{\Gamma}}$$

One then has

$$\frac{\partial}{\partial\tilde{\Gamma}} = \frac{\partial\Gamma}{\partial\tilde{\Gamma}}\frac{\partial}{\partial\Gamma} = (1-\Gamma)^2\frac{\partial}{\partial\Gamma} \tag{A6}$$

and

$$\frac{\partial^2}{\partial\tilde{\Gamma}^2} = (1-\Gamma)^2\frac{\partial}{\partial\Gamma}\left[(1-\Gamma)^2\frac{\partial}{\partial\Gamma}\right]$$

$$= (1-\Gamma)^4\frac{\partial^2}{\partial\Gamma^2} - 2(1-\Gamma)^3\frac{\partial}{\partial\Gamma} \tag{A7}$$

Inserting these formulas into eqs A4 and A5 and using the results in eq A3, one obtains

$$\left[\sin^2(\theta) + \sinh^2\left(\frac{\Gamma}{1-\Gamma}\right)\right]\frac{\partial C_i}{\partial\tau} = \mathcal{D}_i\left\{\frac{\partial^2 C_i}{\partial\theta^2} - \tan(\theta)\frac{\partial C_i}{\partial\theta} + (1-\Gamma)^4\frac{\partial^2 C_i}{\partial\Gamma^2} + \left[(1-\Gamma)^2\tanh\left(\frac{\Gamma}{1-\Gamma}\right) - 2(1-\Gamma)^3\right]\frac{\partial C_i}{\partial\Gamma}\right\} + Z_i\left(C_i\left\{\frac{\partial^2\Psi}{\partial\theta^2} - \tan(\theta)\frac{\partial\Psi}{\partial\theta} + (1-\Gamma)^4\frac{\partial^2\Psi}{\partial\Gamma^2} + \left[(1-\Gamma)^2\tanh\left(\frac{\Gamma}{1-\Gamma}\right) - 2(1-\Gamma)^3\right]\frac{\partial\Psi}{\partial\Gamma}\right\} + \frac{\partial C_i}{\partial\theta}\frac{\partial\Psi}{\partial\theta} + (1-\Gamma)^4\frac{\partial C_i}{\partial\Gamma}\frac{\partial\Psi}{\partial\Gamma}\right)$$

To obtain boundary conditions along the electrode ($\Gamma = \tilde{\Gamma} = 0$ and $0 \le \theta \le \pi/2$), one notes from the formulas A2 and A6 that on the electrode

$$\nabla C_i \cdot \mathbf{n} = \frac{\partial C_i}{\partial Y} = \frac{1}{\sin(\theta)}\frac{\partial C_i}{\partial\Gamma}$$

so that

$$\mathbf{N}_i \cdot \mathbf{n} = \frac{-c_1^\infty D_1}{a\sin(\theta)}\left(\mathcal{D}_i\frac{\partial C_i}{\partial\Gamma} + Z_i C_i\frac{\partial\Psi}{\partial\Gamma}\right) \tag{A8}$$

Similarly, on the insulating container wall ($\theta = 0$ and $0 < \Gamma \le 1$) one finds

$$\mathbf{N}_i \cdot \mathbf{n} = \frac{-c_1^\infty D_1}{a\sinh[\Gamma/(1-\Gamma)]}\left(\mathcal{D}_i\frac{\partial C_i}{\partial\theta} + Z_i C_i\frac{\partial\Psi}{\partial\theta}\right) \tag{A9}$$

and on the line of symmetry through the center of the disk ($r = 0$, $\theta = \pi/2$, and $0 < \Gamma \le 1$)

$$\mathbf{N}_i \cdot \mathbf{n} = \frac{-c_1^\infty D_1}{a\cosh[\Gamma/(1-\Gamma)]}\left(\mathcal{D}_i\frac{\partial C_i}{\partial\theta} + Z_i C_i\frac{\partial\Psi}{\partial\theta}\right) \tag{A10}$$